

How Accurate Is Poisson–Boltzmann Theory for Monovalent Ions near Highly Charged Interfaces?

Wei Bu, David Vaknin,* and Alex Travesset

Ames Laboratory and Department of Physics and Astronomy, Iowa State University, Ames, Iowa 50011

Received December 15, 2005. In Final Form: April 8, 2006

Surface sensitive synchrotron X-ray scattering studies were performed to obtain the distribution of monovalent ions next to a highly charged interface. A lipid phosphate (dihexadecyl hydrogen-phosphate) was spread as a monolayer at the air–water interface to control surface charge density. Using anomalous reflectivity off and at the L_3 Cs^+ resonance, we provide spatial counterion (Cs^+) distributions next to the negatively charged interfaces. Five decades in bulk concentrations are investigated, demonstrating that the interfacial distribution is strongly dependent on bulk concentration. We show that this is due to the strong binding constant of hydronium H_3O^+ to the phosphate group, leading to proton-transfer back to the phosphate group and to a reduced surface charge. The increase of Cs^+ concentration modifies the contact value potential, thereby causing proton release. This process effectively modifies surface charge density and enables exploration of ion distributions as a function of effective surface charge-density. The experimentally obtained ion distributions are compared to distributions calculated by Poisson–Boltzmann theory accounting for the variation of surface charge density due to proton release and binding. We also discuss the accuracy of our experimental results in discriminating possible deviations from Poisson–Boltzmann theory.

I. Introduction

The theoretical determination of ion distributions in aqueous solutions was initiated almost a century ago by Guoy¹ and Chapman,² who applied the Poisson–Boltzmann (PB) theory to calculate the spatial distribution of monovalent ions near a uniformly charged interface. Ever since their seminal work, the topic remains central in statistical mechanics, physical chemistry, and biophysics.³ The original PB theory is a mean field theory with some simplified assumptions such as point like particles and uniform surface charge density. To account for the finite ionic radius, Stern introduced phenomenologically a layer of ions at the charged interface with a different dielectric constant, the Stern layer.⁴ The effect of excess salt concentration and the resulting screening was extended by Debye–Hückel.⁵ Grahame generalized the Gouy–Chapman theory to multivalent ions.⁶ Subsequently, more refined theories and numerical simulations were developed to incorporate short-range interactions, image charges, finite size ionic radius, and ion–ion correlations.^{7–10} More recently, modifications of PB theory have been developed to incorporate hydration forces.^{11–13} Some first-principles calculations of surface-tension for amphiphilic monolayers assume a PB theory with one or more layers of varying dielectric constant.¹⁴

Experimental support for the validity of PB theory was provided by electrokinetic, visco-electric effects, and other techniques

(see Ref 15 for a review). McLaughlin and collaborators¹⁶ have shown good agreement between ζ potentials computed from PB theories and electrophoretic measurements in lipid vesicles. Other techniques, such as radiotracer experiments,^{17–19} X-ray reflectivity,^{20–22} or infrared spectroscopy,²³ allow the determination of the total amount of ions in the immediate vicinity of a charged interface. It is noteworthy that all of the experimental data for monovalent ions (at moderate salt concentrations ≤ 0.1 M) outlined above are adequately described by the Guoy–Chapman theory (with the generalization of excess salt) with no need for further corrections.^{21,24} A close inspection, however, shows the agreement between theory and experiment is either based on fitting variables such as surface charge or interfacial dielectric values that are not known in advance and/or based on integrated quantities. As an example, it has been shown recently that the degree of proton dissociation of arachidic acid spread on a sodium salt solution is adequately described by PB theory, but this agreement only involves the integral (over the entire space) of the sodium distribution.^{23,24} Thus, local deviations that preserve the integral of the distribution (i.e., total number of ions) are not discriminated by these experiments. On the other hand, force measurements between two charged membranes separated by salt solutions, although well described by PB theory at large distances, show strong deviations at short distances (1–2 nm).^{3,11} The origin of these hydration forces is still controversial. In some cases, it has been suggested to extend PB theory to incorporate the restructuring of water, resulting in ion distributions

* To whom correspondence should be addressed.

- (1) Guoy, A. *J. Phys.* (Paris) **1910**, 9, 457.
- (2) Chapman, D. L. *Philos. Mag.* **1913**, 25, 475.
- (3) Israelachvili, J. *Intermolecular and surface forces*, Academic Press: London, 2000.
- (4) Stern, O. *Z. Elektrochem.* **1924**, 30, 508.
- (5) Debye, P. P.; Hückel, F. *Phys. Z.* **1923**, 24, 185.
- (6) Grahame, D. C. *Chem. Rev.* **1947**, 1, 103.
- (7) Outhwaite, C. J. *Chem. Soc. Faraday* **1978**, 74, 1214.
- (8) Outhwaite, C.; Bhuiyan, L. B.; Levine, S. J. *Chem. Soc. Faraday II* **1980**, 76, 1388.
- (9) Torrie, G. M.; Valleau, J. P.; Patey, G. N. *J. Chem. Phys.* **1982**, 76, 4615.
- (10) Kjellander, R.; Marcelja, S. *J. Chem. Phys.* **1984**, 82, 2122.
- (11) Leikin, S.; Parsegian, V.; Rau, D. C. *Annu. Rev. Phys. Chem.* **1993**, 44, 369.
- (12) Manciu, M.; Ruckenstein, E. *Adv. Colloid Interface Sci.* **2004**, 112, 109.
- (13) Faraudo, J.; Bresme, F. *Phys. Rev. Lett.* **2004**, 92, 236102.
- (14) Proesser, A. J.; Franses, E. I. *Colloids Surf. A* **2001**, 178, 1.

- (15) Hunter, R. J. *Colloid Science*; Academic Press: London, 1981.
- (16) McLaughlin, S. *Annu. Rev. Biophys. Chem.* **1989**, 18, 113.
- (17) Tajima, K. *Bull. Chem. Soc. Jpn.* **1971**, 44, 1767.
- (18) Tajima, K.; Muramatsu, K.; Sasaki, M. *Bull. Chem. Soc. Jpn.* **1970**, 43, 1991.
- (19) Kobayashi, K.; Takaoka, K. *Bull. Chem. Soc. Jpn.* **1986**, 59, 93.
- (20) Kjaer, K.; Als-Nielsen, J.; Helm, C.; Tippman-Krayer, P.; Möhwald, H. *J. Phys. Chem. Phys.* **1989**, 93, 3200.
- (21) Bloch, J. M.; Yun, W. *Phys. Rev. A* **1990**, 41, 844.
- (22) Bedzyk, M. J.; Bommarito, G. M.; Caffrey, M.; Penner, T. L. *Science* **1990**, 248, 52.
- (23) LeCalvez, E.; Blaudez, D.; Buffeteau, T.; Desbat, B. *Langmuir* **2001**, 17, 670.
- (24) Travesset, A.; Vaknin D. *Europhys. Lett.* **2006**, 74, 181.

that deviate from PB at short distances from the interface.^{12,25,26} It is therefore imperative to determine the ion distribution itself to establish the degree of accuracy of PB theory.

In this manuscript, we experimentally determine the distribution of Cs⁺ ions next to charged interfaces by anomalous X-ray reflectivity^{27,28} for several decades in bulk cesium concentrations. We compare our results with the predictions of PB theory and present a discussion on the sensitivity of the experimental results to quantify the magnitude of possible deviations from the PB distribution. This kind of investigation has become feasible only with the advent of the second generation X-ray synchrotron sources with novel insertion devices (i.e., undulator) and improved optics, which readily produce variable-energy X-ray beams with brilliances capable of detecting a single atomic-layer even if not closely packed.

The manuscript is organized as follows: In section II, we review several theoretical results relevant to this study. In section III, the experimental details are provided. In section IV, the X-ray reflectivity (XR) and grazing incidence X-ray diffraction (GIXD) measurements are presented with detailed structural analysis. The experimental results are compared with the theoretical PB theory in section V. The implications of the present study are discussed in section VII.

II. PB Theory Including Proton Transfer and Release

We briefly review the PB theory of an aqueous solution containing monovalent ions (1:1 positive and negative electrolytes) of average bulk concentration n_b in the presence of an ideally flat charged interface of known surface density $\sigma_0 = -en_0$, at $z = 0$. As the surface charge is uniformly distributed, the electric potential ψ depends only on the distance from the interface z , and the Boltzmann distribution is

$$\rho(z) = en_b[e^{-e\psi(z)/k_B T} - e^{e\psi(z)/k_B T}] = -2en_b \sinh(\phi(z)) \quad (1)$$

where k_B is the Boltzmann constant and $\phi(z) = e\psi(z)/k_B T$. The ion distribution is calculated self-consistently from the Poisson equation

$$d^2\phi/dz^2 = \sinh\phi/\lambda_D^2 \quad (2)$$

where $\lambda_D = (\epsilon k_B T / 8\pi e^2 n_b)^{1/2}$ is the Debye screening length. Equation 2 can be solved analytically, yielding

$$\psi(z) = -\frac{2k_B T}{e} \ln \left[\frac{1 + \gamma e^{-z/\lambda_D}}{1 - \gamma e^{-z/\lambda_D}} \right] \quad (3)$$

$$n^+(z) = n_b \left(\frac{1 + \gamma e^{-z/\lambda_D}}{1 - \gamma e^{-z/\lambda_D}} \right)^2 \quad (4)$$

where $\gamma = \tanh[e\psi(0)/4k_B T] = -\lambda_{GC}/\lambda_D + ((\lambda_{GC}/\lambda_D)^2 + 1)^{1/2}$, and $\lambda_{GC} = k_B T e / 2\pi\sigma_0 e$ is the Gouy–Chapman length. Figure 1A shows calculated counterion distributions using eq 4 for a fixed surface charge density, typical of fully deprotonated closed packed phospholipids $\sigma_0 = -e/40 \text{ \AA}^2$ for several salt concentrations. It is worth noting that for this surface density ($\lambda_{GC} \approx 0.9 \text{ \AA}$) and bulk salt concentrations ($\lambda_D = 963.5$ and 9.6 \AA at 10^{-5} and 0.1 M , respectively) ($\lambda_{GC}/\lambda_D \ll 1$, and $\gamma \approx 1 - (\lambda_{GC}/\lambda_D)$), the concentration of ions next to the interface is independent of bulk concentration

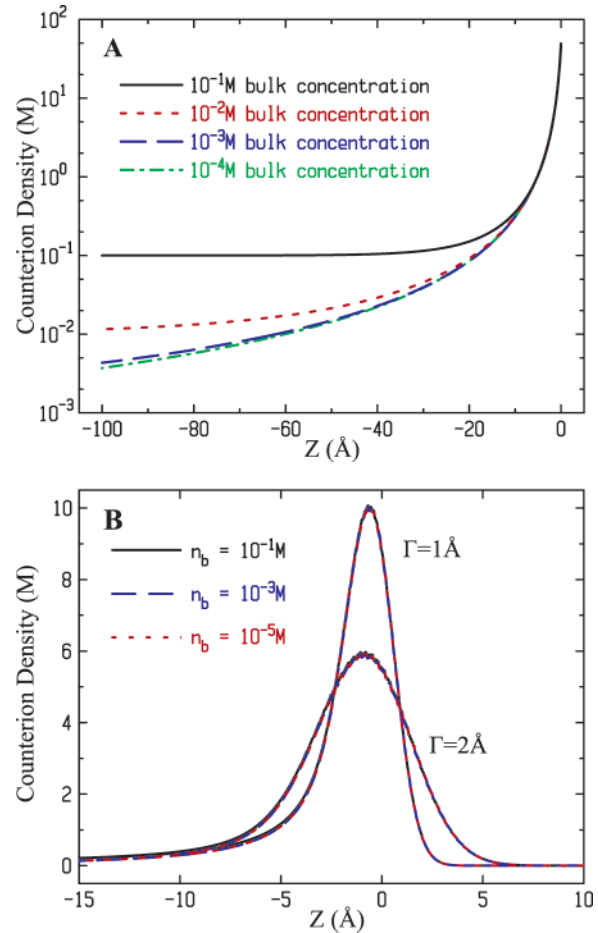


Figure 1. (A) Calculated monovalent ion distributions $n^+(z)$ near a negatively charged surface as obtained from PB theory, eq 4 for different bulk concentration. Surface charge density σ_0 is one electron charge per 40 \AA^2 , $\epsilon = 80$, and $T = 292 \text{ K}$. Note that for this surface charge density the value of the distribution at the $z = 0$ is practically a constant, $n^+(0) \approx (2\pi\sigma_0^2/k_B T \epsilon)$ (B) The convolutions of the distributions $n^+(z)$ using eq 7 assuming two Γ values as indicated. For this strongly charged surface the convoluted distributions for different bulk ionic concentrations are practically indistinguishable.

$$n(z) \approx \frac{\epsilon k_B T}{2\pi e^2 (z + \lambda_{GC})^2}; \quad \text{for } \frac{z}{\lambda_D} \ll 1 \quad (5)$$

We have recently argued²⁸ that theoretical PB distributions should be convoluted with the experimental resolution function $R(z)$ for comparison with experiments, as follows:

$$n_r^+(z) = \int n^+(z') R(z' - z) dz' \quad (6)$$

In the particular case of a Gaussian resolution function, the convolution is

$$n_r^+(z) = \frac{1}{\Gamma\sqrt{2\pi}} \int n^+(z') e^{-[(z-z')^2/2\Gamma^2]} dz' \quad (7)$$

The width in the Gaussian function is given as a sum, $\Gamma = (\sum \Gamma_i^2)^{1/2}$, where each Γ_i 's account for surface-roughness due to capillary waves and imperfections in the monolayer and other contributions. Since surface roughness is the dominant contribution, we use $\Gamma \approx \xi_{\text{Ref}}$, where ξ_{Ref} is the average roughness determined from the reflectivities. From the statistical mechanical perspective, the above convolution may be justified if the fluctuations of the interface are Gaussian and the wavelength of

(25) Gur, Y.; Ravina, I.; Babchin, A. J. *J. Colloid Interface Sci.* **1978**, *64*, 333.

(26) Paunov, V. N.; Dimova, R. I.; Kralchevsky, P. A.; Broze, G.; Mehreteab, A. *J. Colloid Interface Sci.* **1996**, *182*, 239.

(27) Vaknin, D.; Krüger, P.; Lösche, M. *Phys. Rev. Lett.* **2003**, *90*, 178102.

(28) Bu, W.; Vaknin, D.; Travesset, A. *Phys. Rev. E* **2005**, *72*, 060501.

the capillary waves Λ is large ($\Lambda \gg \delta$, where δ is typical ion size) so that the ions “see” an effective flat charged interface. Alternative methods for computing distributions next to flexible interfaces have recently been proposed.²⁹ Figure 1B shows convolution of the distributions shown in Figure 1A for two different values of Γ as indicated. It is interesting to note that the convoluted calculations are practically indistinguishable as a function of bulk salt concentration. In section V, we discuss quantitatively to what extent the experimental resolution limits our ability to compare with theoretical distributions.

The system we describe in this paper differs from simple PB in that one of the ions species, the hydronium H_3O^+ , can bind to the interface, and as a result, out of the N_p phosphate groups forming the interface, only αN_p are electrically charged. The density of charge in the system (including the interfacial charge $z = 0$) is therefore

$$\rho(z) = e \sum_a q_a n_a(z) - e \alpha n_0 \delta(z) \quad (8)$$

The index a runs over the different species of ions present in solution and $q_a = \pm 1$ is their valence (i.e., the solution contains monovalent ions only). In the free energy, the ions are treated as an ideal gas within the solvent and subjected to electrostatic contributions (the standard PB).³⁰ We also incorporate two additional terms that represent the favorable binding of hydroniums to the interface and the mixing entropy of the charged and neutral phosphate groups at the interface

$$F = \frac{1}{2} \int d^3\mathbf{r} \int d^3\mathbf{r}' \frac{\rho(\mathbf{r})\rho(\mathbf{r}')}{|\mathbf{r}-\mathbf{r}'|} + k_B T \sum_a \int d^3\mathbf{r} n_a(\mathbf{r}) (\log(v n_a(\mathbf{r})) - 1) - E_H (1 - \alpha) N_p - k_B T \log \left(\frac{N_p!}{(\alpha N_p)! ((1 - \alpha) N_p)!} \right) \quad (9)$$

where E_H is the gain in free energy for a hydronium binding to the phosphate group. The quantity v has dimensions of volume and defines the standard state.

The condition that the free energy is a minimum for variations of the different number densities $n_a(\mathbf{r})$ under the constraint of a fixed number of particles (canonical ensemble) leads to the Boltzmann distribution $n_a(z) = v^{-1} e^{(\mu_a/k_B T)} e^{-q_a(e\psi(z)/k_B T)}$ with chemical potential $\mu_a = k_B T \log(n_a^b v)$, and also to the Poisson equation, eq 2. Further minimization of the free energy with respect to the parameter α yields the additional equation

$$E_H/k_B T - \phi(0) + \log(\alpha N_p) - \log((1 - \alpha) N_p) = -\mu_H/k_B T \quad (10)$$

where $\psi(0)$ is the value of the electric potential at the interface (the contact value). This equation may be rewritten as

$$n_H^b v e^{-\phi(0)} \frac{\alpha}{1 - \alpha} = e^{-(E_H/k_B T)} \quad (11)$$

and expresses the equilibrium of the process $\text{H}_3\text{O}^+ + \text{PO}_4^- \leftrightarrow \text{PO}_4\text{H}^0 + \text{H}_2\text{O}$.³¹ If the standard state is defined as $v = 1$ molar, the binding free energy E_H is related to the $\text{p}K_a$ of the molecules forming the interface by $E_H = k_B T \log K_a$ and the hydronium

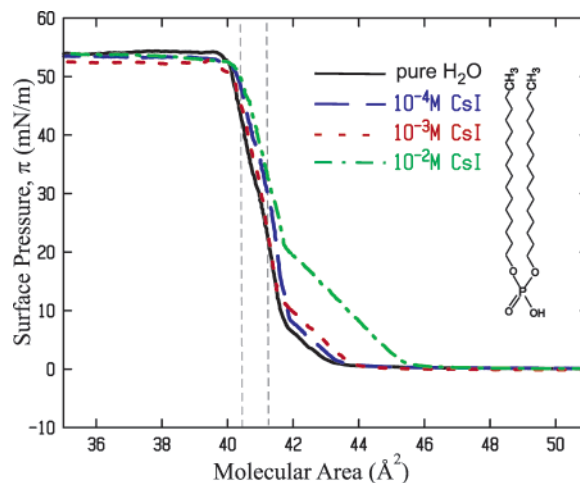


Figure 2. Surface pressure versus molecular area for DHDP spread on CsI solutions at various concentrations as indicated. Reflectivity and GIXD were performed at constant surface-pressures 30 and 40 mN/m.

concentration is related to the pH of the solution by $n_H = 10^{-\text{pH}}$. Substitution of these values into eq 11 yields

$$10^{-\text{pH}} e^{-\phi(0)} \frac{\alpha}{1 - \alpha} = 10^{-\text{p}K_a} \quad (12)$$

The fraction of charged phosphate groups is then

$$\alpha = \frac{1}{1 + 10^{-(\text{pH} - \text{p}K_a)} e^{-\phi(0)}} \quad (13)$$

As a result, the PB equation, eq 2, needs to be solved with the self-consistent boundary condition, eq 13

$$\sinh\left(\frac{\phi(0)}{2}\right) = -\left(\frac{\lambda_D}{\lambda_{GC}}\right) \frac{1}{1 + 10^{-(\text{pH} - \text{p}K_a)} e^{-\phi(0)}} \quad (14)$$

The ion distribution is given by eq 4 with a renormalized Guoy-Chapman length $\lambda'_{GC} = \lambda_{GC}/\alpha$ (RPB). At high surface charge, the contact point potential is significantly larger than $k_B T$, and the consequences of eq 14 are dramatic. The ion distribution becomes strongly dependent on ion concentration for points very close to the interface, as shown in Figure 10. This should be contrasted with Figure 1, where the ion distribution is independent of bulk concentration.

III. Experimental Details

To manipulate ion bulk-concentrations, we used CsI (99.999%, Sigma Corp., catalog no. 203033) solutions in ultrapure water, taking advantage of the L_3 resonance of Cs ions at 5.012 keV in anomalous reflectivity measurements. To control surface charge density, monolayers of dihexadecyl-hydrogen-phosphate (DHDP, see Figure 2; $\text{C}_{32}\text{H}_{67}\text{O}_4\text{P}$; MW = 546.86, Sigma Corp., catalog no. D2631) were spread from 3:1 chloroform/methanol solutions at the air–water interface in a thermostated Langmuir trough.³² DHDP was chosen for this study, since it forms a simple in-plane structure at high enough surface pressures^{33,34} and its hydrogen-phosphate headgroup ($\text{R-PO}_4\text{H}$) has a $\text{p}K_a = 2.1$, presumably guaranteeing almost complete dissociation $[\text{PO}_4^-]/[\text{R-PO}_4\text{H}] \approx 0.99999$, with one electron-charge per molecule ($\sigma_0 \approx 0.4 \text{ C/m}^2$). Monolayers of DHDP were prepared in a thermostatic, solid Teflon Langmuir trough and kept under

(29) Fleck, C. C.; Netz, R. R. *Phys. Rev. Lett.* **2005**, *95*, 128101.

(30) Safran, S. *Statistical thermodynamics of surfaces, interfaces, and membranes*; Frontiers in Physics; Addison-Wesley Publishers: Reading, MA, 1994.

(31) Healy, T. W.; White, L. R. *Adv. Colloid Interface Sci.* **1978**, *9*, 303.

(32) Vaknin, D. *J. Am. Chem. Soc.* **2003**, *125*, 1313.

(33) Gregory, B. W.; Vaknin, D.; Gray, J. D.; Ocko, B. M.; Stroev, P.; Cotton, T. M.; Struve, W. S. *J. Phys. Chem. B* **1997**, *101*, 2006.

(34) Gregory, B. W.; Vaknin, D.; Gray, J. D.; Ocko, B. M.; Cotton, T. M.; Struve, W. S. *J. Phys. Chem. B* **1999**, *103*, 502.

water-saturated helium environment. Ultrapure water (NANOpure, Barnstead apparatus; resistivity, 18.1 M Ω cm) was used for all solution preparations. Monolayer compression, at a rate of $\sim 1 \text{ \AA}^2/(\text{molecule} \times \text{min.})$, was started 10–15 min after spreading to allow solvent evaporation. The monolayer was then compressed to the desired surface pressure. During the compression, the surface pressure was recorded by a microbalance using a filter-paper Wilhelmy plate. The Langmuir trough is mounted on a motorized stage that can translate the surface laterally with respect to the incident beam to allow the examination of different regions of the sample to reproduce results and monitor radiation damage of the monolayer.

X-ray studies of monolayers at gas/water interfaces were conducted on the Ames Laboratory liquid surface diffractometer at the Advanced Photon Source (APS), beam-line 6ID-B (described elsewhere³⁵). The highly monochromatic beam (16.2 and 5.012 keV; $\lambda = 0.765334$ and $\lambda = 2.47374 \text{ \AA}$), selected by a downstream Si double crystal monochromator, is deflected onto the liquid surface to a desired angle of incidence with respect to the liquid surface by a second monochromator [Ge(220) and Ge(111) crystals at 16.2 and 5.012 keV, respectively] located on the diffractometer.^{35,36} Prior to the measurements, the absolute scale of the X-ray energy was calibrated with six different absorption edges to better than $\pm 3 \text{ eV}$.

X-ray reflectivity and GIXD are commonly used to determine the monolayer structure.^{35,37–39} Specular XR experiments yield the electron density profile across the interface, and can be related to molecular arrangements in the film. Herein, the electron density profile across the interface is extracted by a two-stage refinement of a parametrized model that best fits the measured reflectivity by nonlinear least-squares method. A generalized density profile $\rho(z) = \rho'(z) + i\rho''(z)$ of the electron-density (ED) and the absorption-density (AD) (real and imaginary parts, respectively) is constructed by a sum of error functions as follows:

$$\rho(z) = \frac{1}{2} \sum_{i=1}^{N+1} \text{erfc} \left(\frac{z-z_i}{\sqrt{2}\xi_i} \right) (\rho_i - \rho_{i+1}) + \rho_{i+1}/2 \quad (15)$$

where $N + 1$ is the number of interfaces, $\rho_i = \rho'_i + i\rho''_i$, ρ'_i and ρ''_i are the ED and AD of i th slab, z_i and ξ_i are the position and roughness of i th interface, respectively, ρ_1 is the electron density of the solution ($\approx 0.334 \text{ e/\AA}^3$), and $\rho_{N+2} = 0$ is the electron density of the gaseous environment. The use of a different roughness ξ_i for each interface preserves the integral of the profile along Z or the electron density per unit area, thus conserving the chemical content per unit area a . Although small variations are expected in ξ_i for interfaces that separate the rigid portion of a molecule (hydrocarbon chains/gas interface and hydrocarbon chain/headgroup interface, for instance), somewhat larger variations can occur at different interfaces (such as gas/hydrocarbon chains interface versus headgroup/subphase interface). The AD profile is particularly important at the Cs resonance (5.012 keV) as demonstrated below. The reflectivity is calculated by recursive dynamical methods^{40,41} of the discretized ED and AD in eq 15. In the first stage of the refinement, the variable parameters used to construct the electron density across the interface $\rho(z)$ are the thickness values of the various slabs $d_i = |z_{i+1} - z_i|$, their corresponding electron densities ρ_i , and interfacial roughness ξ_i . By nonlinear square fit (NLSF), we determine the minimum number of slabs or “boxes” required for obtaining the best fit to the measured reflectivity. The minimum number of slabs is the one for which the addition of another slab does not improve the quality of the fit, i.e., does not improve χ^2 . In the second stage, we apply space filling and

volume constraints^{33,44,45} to calculate ρ_i by assigning to each slab a different portion of the molecule, the ions, and water molecules to a profile that has the same number of slabs as obtained in stage one of the analysis. As described in detail in section IV, the model eliminates the ρ_i 's as parameters and is self-consistent with the molecular structure, providing detailed information on the constituents of each slab.

The GIXD measurements are conducted to determine the lateral organization in the film. The angle of the incident beam with respect to the surface, α , is fixed below the incident and reflected critical angle ($\alpha_c = \lambda(\rho_s r_0/\pi)^{1/2}$; $r_0 = 2.82 \times 10^{-13} \text{ cm}$, where ρ_s is the electron density of subphase) for total reflection, while the diffracted beam is detected at a finite azimuthal in-plane angle, 2Θ , and out-of plane, β (the angle of the reflected beam with respect to the surface). Rod scans along the surface normal at the 2D Bragg reflections are used to determine the average ordered chain length and tilt with respect to the surface normal. The intensity along the rod of the 2D Bragg reflection is analyzed in the framework of the distorted wave Born approximation (DWBA)

$$I(Q_{xy}, Q_z) \approx |t(k_{z,i})|^2 |F(Q_z)|^2 |t(k_{z,f})|^2 \quad (16)$$

where $t(k_{z,i})$ and $t(k_{z,f})$ ($k_{z,i} = k_0 \sin \alpha$; $k_{z,f} = k_0 \sin \beta$) are the Fresnel transmission functions, which give rise to an enhancement at the critical angle. In modeling the rod scans, the length and tilt of the tails are varied, examining two tilt directions: one toward nearest neighbors (NN) and the second toward next NN (NNN).^{39,46} The form factor for the tails is given by

$$F(Q_z) = \sin(Q_z l/2)/(Q_z l/2) \quad (17)$$

where Q_z is defined along the long axis of the tail, and l is the length of the tail.

IV. Experimental Results

A. Isotherm Comparisons. Surface pressure versus molecular-area ($\pi - A$) isotherms of DHDP at various CsI salt concentrations (n_b) are shown in Figure 2. For $\pi > 0$, the isotherm exhibits two distinct slopes, associated with crystalline tilted and untilted acyl-chains with respect to the surface normal. The transition from tilted to untilted chains at (A_t, π_t), occurs at a constant $A_t \approx 41.5 \text{ \AA}^2$, whereas π_t increases with salt concentration n_b . CsI and other electrolytes (NaCl and CsCl) in solution significantly influence the isotherm causing an increase of the monolayer-coalescence area A_C , (i.e., $\pi > 0$) with the increase in n_b . For $A \lesssim 39 \text{ \AA}^2$, approximately the cross-section of the two acyl-chains of DHDP, (constant $\pi \approx 55 \text{ mN/m}$) the monolayer is in the yet poorly characterized state of *collapse*. In the present study we focus on the untilted crystalline phase ($30 \lesssim \pi \lesssim 45 \text{ mN/m}$), where the molecular area variation at a fixed π is less than 1.5% (in the data analysis we allow $\pm 5\%$ variation in molecular area).

B. GIXD and Reflectivity off Resonance. GIXD experiments provided additional insight into the molecular packing of the acyl chains within the Langmuir monolayers, namely, the average inplane density of the headgroups and the surface charge-density. Figure 3 shows GIXD scans from DHDP on pure water and on CsI solution (10^{-3} M , at $\pi = 30 \text{ mN/m}$) and from bare surface

(35) Vaknin, D. in *Methods in Materials Research*; Kaufmann, E. N., et al., Eds.; Wiley: New York, 2001; p 10d.2.1.

(36) Als-Nielsen, J.; Pershan, P. S. *Nucl. Instrum. Methods Phys. Rev.* **1983**, 208, 545.

(37) Als-Nielsen, J.; Kjaer, K. in *Phase Transitions in Soft Condensed Matter*; Riste, T., Sherrington, D., Eds.; Plenum: New York, 1989.

(38) Jacquemain, D.; Wolf, S. G.; Leveiller, F.; Deutsch, M.; Kjaer, K.; Als-Nielsen, J.; Lahav, M.; Leiserowitz, L. *Angew. Chem.* **1992**, 31, 130.

(39) Kjaer, K. *Physica B* **1994**, 198, 100.

(40) Parratt, L. G. *Phys. Rev.* **1954**, 59, 359.

(41) Born, M.; Wolf, E. *Principles of Optics*; MacMillan: New York, 1959.

(42) Lavoie, H.; Blaudez, D.; Vaknin, D.; Desbat, B.; Ocko, B. M.; Salesse, C. *Biophys. J.* **2002**, 83, 3558.

(43) The 3 density parameters ρ_i are now replaced by 5 parameters in eqs 18 and 20 (N_{Cs^+} , N_{H_2O} , in the headgroup slab and the slab below, and the molecular area A which is restricted to $41 \pm 2 \text{ \AA}^2$). The two volume constraints in eq 22 compensate for the use of two extra parameters.

(44) Vaknin, D.; Kjaer, K.; Als-Nielsen, J.; Lösche, M. *Biophys. J.* **1991**, 59, 1325.

(45) Vaknin, D.; Kjaer, K.; Als-Nielsen, J.; Lösche, M. *Makromol. Chem., Macromol. Symp.* **1991**, 46, 383.

(46) Kaganer, M. V.; Möhwald, H.; Dutta, P. *Rev. Mod. Phys.* **1999**, 71, 779.

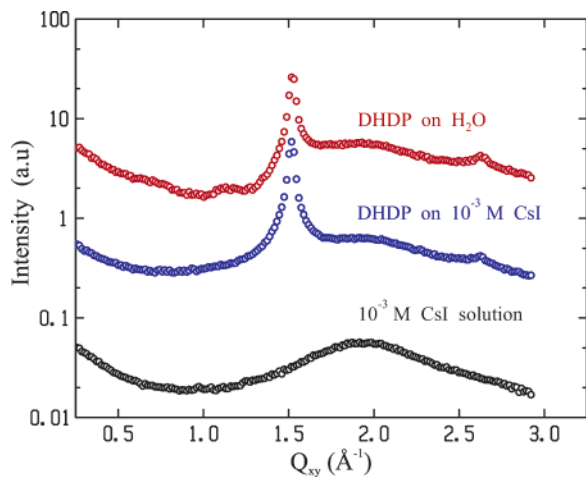


Figure 3. GIXD scans versus the modulus of the inplane momentum transfer Q_{XY} , at surface pressure $\pi = 30$ mN/m (curves are shifted by a decade for clarity). The Bragg peaks are independent of bulk salt concentration indicating no significant change in in-plane molecular packing. GIXD scan for 10^{-3} M CsI (without DHDP) shows a broad peak at $Q_{XY} \approx 2.0$ \AA^{-1} , due to the surface structure of water.

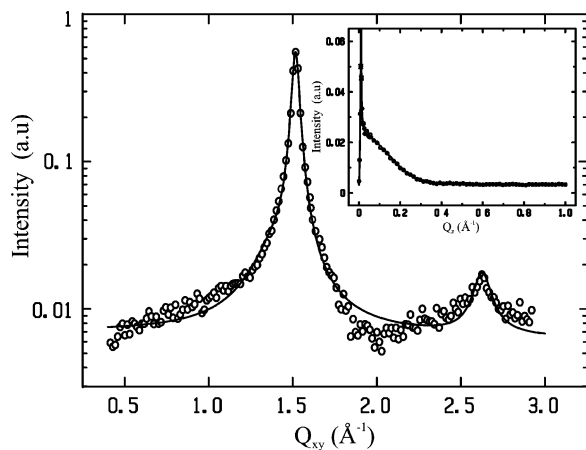


Figure 4. Background subtracted GIXD pattern for a DHDP monolayer on 10^{-3} M CsI solution ($\pi = 30$ mN/m) and the corresponding rod scan (shown in the inset) at the (1,0) peak ($Q_{XY} = 1.516$ \AA^{-1}).

of CsI solution (10^{-3} M) before spreading the monolayer as a function of in-plane momentum transfer $Q_{XY} = (Q_X^2 + Q_Y^2)^{1/2}$.⁴⁷ The broad peak centered at $Q_{XY} \approx 2$ \AA^{-1} is due to the structure-factor of the aqueous–solution interface. The spreading and compression of the monolayer slightly modifies the water structure factor peak at $Q_{XY} \approx 2$ \AA^{-1} , and brings about two prominent Bragg reflections due to the ordering of acyl-chains superimposed on a modified surface liquid structure factor.³² The main features of the diffraction pattern are independent of ionic concentration, consistent with the isotherms at the 30–40 mN/m region that show very small variations in the molecular packing. Figure 4 shows the 2D diffraction pattern consists of a strong Bragg reflection at $Q_{XY} = 1.516$ \AA^{-1} and a weaker peak at $Q_{XY} = 2.627$ \AA^{-1} , corresponding to 4.145, and 2.392 \AA d spacings, respectively (Table 1). The shape, spacing, and location of the two intense peaks correspond closely with literature values for (1,0) and

(47) The coordinate system used in this manuscript is such that Q_Z is normal to the liquid surface, Q_X is parallel to the horizontal (untilted) incident X-ray beam, and Q_Y is orthogonal to both Q_X and Q_Z . The hydrocarbon chains form two-dimensional poly-crystals giving rise to a diffraction pattern that depends on the modulus of the in-plane momentum transfer $Q_{XY} = (Q_X^2 + Q_Y^2)^{1/2}$ and is practically independent of sample rotation over the Z axis.

Table 1. Best-Fit Parameters to High-Resolution Diffraction Scans of DHDP on 10^{-3} M CsI Solution ($\pi = 30$ mN/m)

peak	Q_{XY} (\AA^{-1})	Δ (\AA^{-1})	intensity (a.u)
(1,0)	1.516 ± 0.003	0.026	0.522
(1,1)	2.627 ± 0.024	0.060	0.009

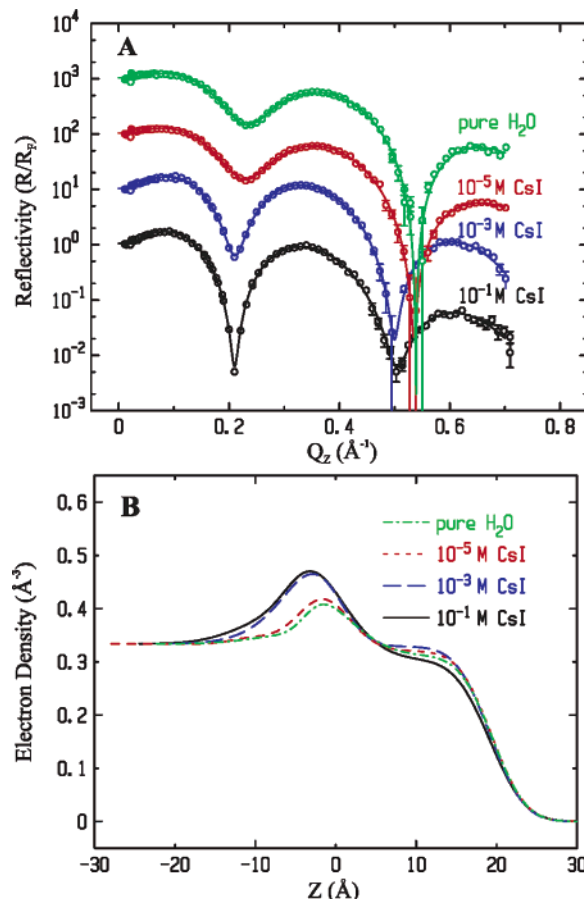


Figure 5. (A) X-ray reflectivity (circles) and corresponding best fit (solid lines) for the DHDP monolayer at four solutions ($\pi = 40$ mN/m) (curves are shifted by a decade for clarity). (B) ED profiles used to calculate the fits shown in (A).

(1,1) planes in a hexagonal unit cell of ordered alkyl chains, also confirmed by the ratio $Q_{XY}(1,1)/Q_{XY}(1,0) = \sqrt{3}$. This unit cell (molecular area 19.83 \AA^2) agrees with the cross-sectional area of alkyl chain.⁴⁶ Each headgroup has two alkyl chains, giving a molecular area of 39.66 \AA^2 , in agreement with values obtained from the π - A isotherm (~ 40.5 \AA^2 , $\pi = 40$ mN/m). The small variations in molecular areas are attributed to the existence of domain boundaries, defects, and minute impurities. The peaks in Figure 4 were fitted to Lorentzians the parameters of which are given in Table.1. The peak line width Δ is significantly larger for the higher order peak. This is expected in simple 2D crystals⁴⁸ and is even more pronounced for 2D crystals fluctuating in 3D space (fluctuating tethered membranes, see ref 49). The inset in Figure 4 shows the rod-scan at $Q_{XY}(1,0)$ Bragg reflection. The rod-scan analysis (using eqs 16 and 17) yields an average chain-length ~ 20 \AA , and a tilted angle with respect to the surface normal $< 5^\circ$, consistent with the reflectivity and previous reports.³⁴

Figure 5A shows the normalized reflectivity curves, R/R_F (where R_F is the calculated reflectivity of an ideally flat subphase interface), for DHDP ($\pi = 40$ mN/m) on pure H_2O and CsI solutions measured at $E = 16.2$ keV. The solid lines are the best-fit calculated reflectivities based on the ED profiles shown

(48) Jancovici, B. *Phys. Rev. Lett.* **1967**, *19*, 20.

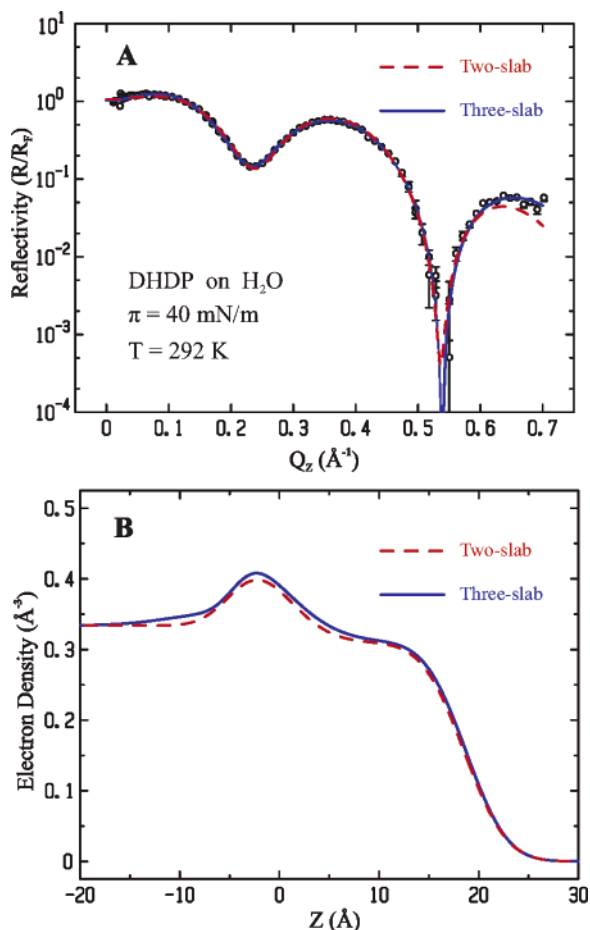


Figure 6. (A) Reflectivity (circles) taken from DHDP on pure H₂O and the best fit by using two-slab model (dashed line) and three-slab model (solid line). (B) ED profiles extracted from two-slab and three-slab model.

in Figure 5B. Similar reflectivity curves were obtained for $\pi = 30$ mN/m. In Figure 5A, all X-ray reflectivity curves differ in the exact position and the sharpness of their minima, and the intensities of their maxima. Given that, as already shown, the packing of DHDP is basically independent of salt concentration for $\pi = 40$ mN/m, the reflectivity curves in Figure 5A qualitatively show a strong dependence of ion distribution close to the interface on bulk ion concentration, in quantitative agreement with RPB theory as discussed above.

In the first stage of the analysis, we find that the 3-slab ($N = 3$) model provides good quality fit to all reflectivities, and it does not improve with the addition of more slabs, i.e., more parameters. Our measured reflectivity for DHDP on pure H₂O is consistent with previous measurements³³ but extends to larger momentum transfers (Q_z), allowing for a more refined structural analysis. Indeed, the two-slab model used in ref 33 which found to be slightly inadequate, particularly at large Q_z and a better fit is achieved by adding an extra slab at the water-headgroup region, as shown in Figure 6. Thus, our detailed analysis of DHDP on pure water, differs from the one reported in ref 33 in which the headgroup resides on a thin layer (4–6 Å thick) of ED that is just slightly larger than that of bulk water (see Table 2). Similar observations were also reported for other monolayers at the gas/water interface and were interpreted as interfacial water restructuring induced by hydrogen bonds.⁴² Further evidence of water restructuring at the interface is also found in the overall GIXD of the interfacial structure-factor of water, especially a decrease in peak intensity at $Q_{XY} \approx 2 \text{ \AA}^{-1}$ is observed.³²

Table 2. Best-Fit Parameters to the Measured Reflectivities of DHDP Monolayers at $\pi = 40$ mN/m that Generate the ED Profiles Across the Interface^a

subphase	H ₂ O	10 ⁻⁵ M CsI	10 ⁻³ M CsI	10 ⁻¹ M CsI
d_{tail} (Å)	18.7(5)	19.6(10)	19.2(8)	20.2(6)
ρ_{tail} (e/Å ³)	0.311(8)	0.320(17)	0.329(14)	0.304(8)
d_{head} (Å)	4.4	3.2	3.8	4.3
ρ_{head} (e/Å ³)	0.476(15)	0.547(27)	0.590(39)	0.624(38)
d_{Cs} (Å)	3.6	9.5	3.3	4.2
ρ_{Cs} (e/Å ³)	0.375(11)	0.347(5)	0.431(14)	0.441(8)

^a In this work, the error estimate (in parentheses) of a parameter is obtained as described in refs 44 and 45 by fixing a parameter at different values away from its optimum and readjusting all other parameters to a new minimum until χ^2 increases by 50%. Thicknesses of head group and Cs box are not well defined due to electron density decay from $z = 0$ to the bulk.

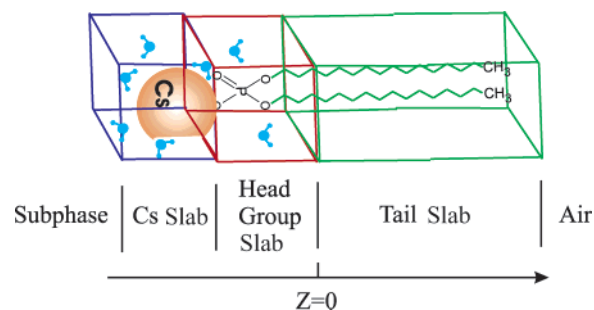


Figure 7. Schematic illustration of the three-slab model used to calculate self-consistently the electron-density profile assuming the a DHDP monolayer of known average molecular area, from GIXD and π -A isotherm, and the associated Cs⁺ and water molecules in the different slabs. Volume constraints were also applied in the ED calculations of the different portions of the molecule and the ion-distribution.

Modeling DHDP monolayers on the salt solution is slightly more complicated as the Cs⁺ concentration decays slowly as a function of distance from the interface. As sketched in Figure 7, we assume that Cs ions are present in both the headgroup slab and the slab contiguous to it toward the bulk of the solution. Table 2 shows the parameters used to produce the ED profiles in Figure 5B, and the best-fit is shown in Figure 5A. The position at $z = 0$ is defined by the interface between the phosphate headgroup and the hydrocarbon chain. ED profiles show that electron densities at and below the phosphate headgroup region are higher with the increase of salt bulk concentration. The small differences of EDs associated with the alkyl-chains for the different subphases are due to the minute variations in molecular areas as shown in the isotherms above.

C. Anomalous Reflectivity. Figure 8A shows reflectivities of DHDP spread on 10⁻³ M CsI for $\pi = 40$ mN/m at 16.2 and 5.012 keV. The reflectivity taken at 16.2 keV has sharper and deeper minima that are slightly shifted to smaller Q_z , compared to the reflectivity taken at 5.012 keV. This is due to the dependence of ρ'_i and ρ''_i on the energy of the X-ray energy. At the two energies that the measurements were conducted (16.2 and 5.012 keV), ρ' and ρ'' dramatically change only for cesium (as shown in Figure 9) and only slightly for the phosphorus ion, whereas for the remaining constituents, the binding energies are smaller than 5.012 keV, and therefore, all electrons behave as free electrons. Here we apply stage two of the analysis, each slab is associated with a portion of the molecule, and the EDs and ADs are calculated self-consistently applying volume constraints. Thus, the ED of the hydrocarbon slab is given by

$$\rho'_{\text{tail}} = N_{\text{tail}}/d_{\text{tail}}A \quad (18)$$

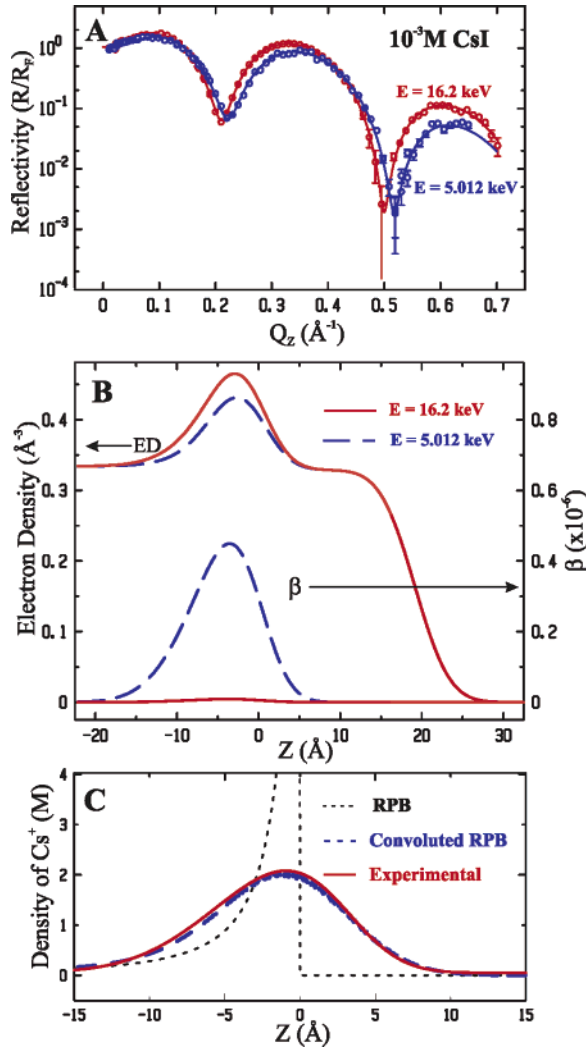


Figure 8. (A) Normalized X-ray reflectivities measured at 16.2 and 5.012 keV for DHDP monolayer spread on 10^{-3} M CsI solution ($\pi = 40$ mN/m). The solid lines are calculated reflectivities using the ED profiles shown in (B). The two data sets were combined and refined to a model with common structural adjustable parameters. Also shown is the profile of absorption factor β , which at 5.012 keV is dominated by the presence of Cs^+ close to the interface. (C) Solid smooth line is the distribution of Cs^+ determined from the reflectivity measurements. The dotted line is the ion distribution calculated from the RPB equation with the corrected surface-charge density due to hydronium affinity to PO_4^- . The dashed line is the RPB result convoluted with a Gaussian of width given by the average surface roughness of the monolayer obtained from XR without any adjustable parameters.

and

$$\rho''_{\text{tail}} = 0 \quad (19)$$

where $N_{\text{tail}} = 258$ is the total number of electrons in the two acyl chains.³³ Similarly, we can calculate ρ_i for the headgroup and for the Cs slabs as follows:

$$\rho'_i = (N_{\text{Cs}^+}Z_{\text{Cs}^+} + N_{\text{H}_2\text{O}}Z_{\text{H}_2\text{O}} + N_{\text{PO}_4^-}Z_{\text{PO}_4^-})/d_iA \quad (20)$$

$$\rho''_i = (\mu_{\text{Cs}^+}N_{\text{Cs}^+}/\rho_{0\text{Cs}} + \mu_{\text{P}}N_{\text{PO}_4^-}/\rho_{0\text{P}})/2d_iA\lambda r_0 \quad (21)$$

where N_j is the number of ions or molecules, Z_j is the number of electrons per ion or molecule, and μ_j is the linear absorption coefficient of the material when the density of material is ρ_{0j} .

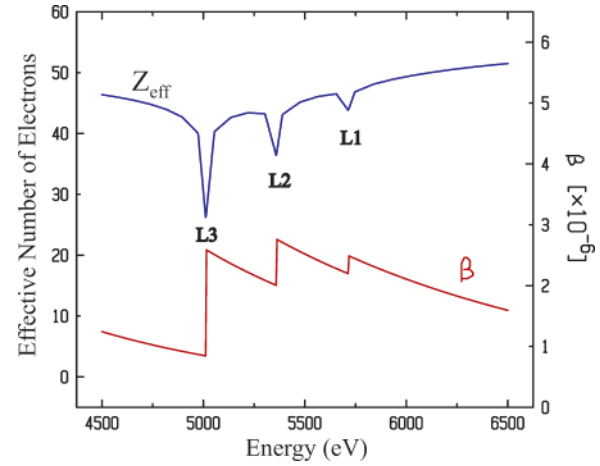


Figure 9. Effective number of electrons and the absorption factor β for Cs^+ . $Z_{\text{eff}} = \rho'/n$, where n is the number density and $\beta = \lambda^2\rho''r_0/2\pi$.

Table 3. Best-Fit Parameters to the Data Sets, in which the Reflectivities Measured at and off Resonance Are Combined, for Various Slab Concentrations at $\pi = 40$ mN/m

subphase (CsI)	10^{-5} M	10^{-4} M	10^{-3} M	10^{-2} M	10^{-1} M
d_{tail} (Å)	19.6	19.8	19.2	18.8	20.2
d_{head} (Å)	3.2	3.7	3.8	6.7	4.3
$N_{\text{Cs}^+}^a$	0.002	0.013	0.270	0.511	0.523
d_{Cs} (Å)	9.5	4.7	3.3	6.9	4.2
$N_{\text{Cs}^+}^b$	0.119	0.288	0.289	0.187	0.410
area (Å ²)	41.00	41.04	40.97	41.00	42.08
total $N_{\text{Cs}^+}^c$	0.12(5)	0.30(7)	0.56(10)	0.70(12)	0.93(12)

^a Number of Cs^+ in the headgroup slab. ^b Number of Cs^+ in the Cs slab. ^c Estimated errors are given in parentheses.

$N_{\text{PO}_4^-} = 1$ in the headgroup slab and $N_{\text{PO}_4^-} = 0$ in the Cs slab (see Figure 7).

Using ρ'_i , ρ''_i and eq 15, we can create the generalized density $\rho(z) = \rho'(z) + i\rho''(z)$, which includes both electron density and absorption density. We then apply the following volume constraints

$$d_iA = N_{\text{Cs}^+}V_{\text{Cs}^+} + N_{\text{H}_2\text{O}}V_{\text{H}_2\text{O}} + N_{\text{PO}_4^-}V_{\text{PO}_4^-}$$

where, $V_{\text{H}_2\text{O}} = 30 \text{ \AA}^3$, $V_{\text{PO}_4^-} = 60 \text{ \AA}^3$ (calculated from the reflectivity of DHDP on water), and $V_{\text{Cs}^+} \approx 20 \text{ \AA}^3$ (calculated from the ionic radius in standard tables).⁴³ The advantage of this method is that a unique set of parameters is used to fit both reflectivities at and off resonance simultaneously, thus providing a strong self-consistency test to the analysis. This is very similar to the approach developed to determine the structure of a phospholipid monolayer by refining neutron and X-ray reflectivities simultaneously.^{44,45}

The solid lines in Figure 8A are calculated from the generalized density $\rho(z)$, obtained from parameters of a single model-structure for the combined data sets, as shown in Figure 8B. The best fit structural parameters obtained by this method for various concentrations of CsI in solution are listed in Table 3. The absorption factor β shown in Figure 8B can be converted to ρ'' , AD curve, by a factor ($\beta = \lambda^2\rho''r_0/2\pi$). The AD curve for 5.012 keV up to a normalization factor is practically the profile of the counterion Cs^+ close to the interface (there is a minute contribution to the AD from phosphorus in the headgroup region, as shown in eq 21). The difference between the EDs at and off resonance, normalized by $Z_{\text{eff}}(16.2 \text{ keV}) - Z_{\text{eff}}(5.012 \text{ keV})$,²⁷ gives the desired ionic distribution at the interface. Figure 8C shows (solid line) the experimental Cs^+ distribution close to the interface at

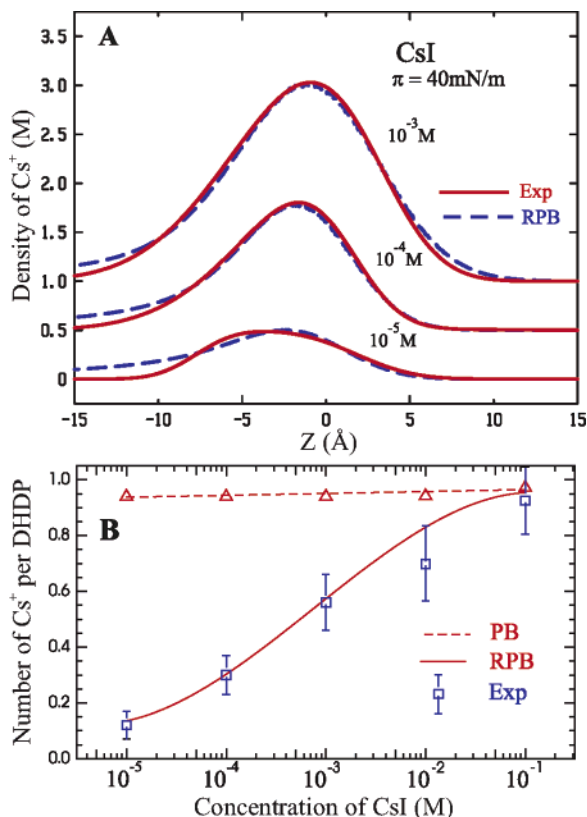


Figure 10. (A) Interfacial Cs⁺ distributions (solid lines) determined from anomalous reflectivities (at 16.2 and 5.012 keV) for various CsI bulk concentration (shifted by 0.5 M for clarity). Calculated and convoluted distributions based on RPB with renormalized surface charge density as described in the text, are shown as dashed lines. (B) Square symbols are numbers of Cs⁺ ions per DHDP ($\approx 41 \text{ \AA}^2$) by integrating (up to 15 Å) the experimental distribution obtained from the anomalous scattering for 10⁻⁵, 10⁻⁴, and 10⁻³ M. For 10⁻² and 10⁻¹ M, the integrated number of ions are determined from the reflectivities off resonance only (the reflectivities at resonance for these concentrations were not measured). The dashed line and the solid line are obtained from PB theory and RPB theory, respectively.

10⁻³ M CsI. Similar distributions corresponding to other bulk CsI concentrations are shown in Figure 10A (solid lines).

V. Comparison of Experimental Results with Theory

A. Ion Distributions. We first compute the integrated number of Cs⁺ per DHDP over the first 15 Å next to the charged interface. This number can be obtained by integrating the experimental distribution along the z axis and can be checked self-consistently from the model used in the analysis of the combined data set (Table 3). The number of ions per DHDP versus CsI bulk concentration are plotted in Figure 10B with square symbols. In Figure 10B, the integrated values obtained by PB theory with the surface charge corresponding to the fully deprotonated phosphate groups is also plotted (triangles connected with a dashed line) for comparison. As shown, the experimental integrated number of Cs⁺ at the interface varies roughly as a power-law of bulk concentration, which is well described with RPB (solid line) without fitting parameters, as described in section II.

The ion distribution predicted from RPB theory using eq 4 with the renormalized Gouy–Chapman length (dashed line) is compared with the experimental distribution in Figures 8C and 10A (solid line). As discussed in section II the theoretical distribution needs to be convoluted with the effective experimental resolution function. The distribution resulting from the convoluted RPB, with no fitting parameters, with Γ ($\Gamma \approx 3.8 \text{ \AA}$) obtained

from the analysis of the reflectivity, is shown to reproduce the experimental data remarkably well, as shown in Figure 8(C). The value for $\text{pH} - \text{p}K_a = 4.5$, used in the calculation, is consistent within the range of our measured values for the $\text{pH} \sim 6.5$.

The distributions corresponding to the three bulk Cs⁺ concentrations 10⁻³, 10⁻⁴, and 10⁻⁵ M are shown in Figure 10A with a solid line. The agreement with the RPB (dashed lines) convoluted as described is remarkable except for points far from the interface. We attribute this error to the difficulty to include slowly decaying tails of the PB theory to the ED profile modeled by the faster decaying Error functions.

B. Possible Deviations from PB Theory Distributions. This section deals with the examination of the sensitivity of the anomalous reflectivity in determining the ion distribution, in addition to the integrated number of ions at the interface. The results presented in Figure 10A show the unique capability of the anomalous reflectivity technique in providing ion distributions. Whereas the integrated number of ions, such as the ones shown in Figure 10B, can be obtained from standard reflectivity measurements and other experimental techniques, as discussed in section I, the determination of ion distributions requires the use of anomalous reflectivity. In fact, data such as that shown in Figure 10B has been used to assess the validity of PB theory in the past. As discussed in the Introduction, the excellent agreement maybe somewhat deceptive in that it may hide significant short-distance deviations from RPB theory because only the total integrated ion density is involved.

Our experimental resolution constrain possible deviations from RPB distributions to within 3.8 Å. If such deviations are nonmonotonic, showing bumps or oscillations, then the constraints are even more stringent. As an example, in Figure 11A, we construct two stepwise distributions ($N = 6$ and $N = 8$ steps of 2.5 and 1.9 Å width, respectively) whose total integrated area is the same as for RPB (continuous line). Although the histograms have the same area as the RPB, they incorporate hypothetical nonmonotonic decay of the distribution in the form of bumps. As it is shown in Figure 11B, despite the fact that the step size are smaller than the 3.8 Å resolution, such distributions can be ruled out by the experiments. This demonstrates that, if actual ion distributions are nonmonotonic, their maxima or minima must be short-ranged in nature (shorter than $\approx 2 \text{ \AA}$) to be consistent with our data.

VI. Conclusions

The goal of this study was to explore the accuracy of PB theory for monovalent ions. For that, we selected a system with a relatively high surface charge density (one electron per 40 Å², lattice constant $\sim 6.8 \text{ \AA}$) and a low $\text{p}K_a = 2.1$ system, which we expected would provide the most favorable scenario to observe deviations from PB theory. From the results obtained in our experiments, we conclude that PB with the renormalization of surface charge density due to proton-transfer and release processes (RPB) is strikingly accurate.

Certainly, the accuracy of our results is limited by the effective experimental resolution, which is dominated by the natural surface-roughness of the gas-amphiphile-water interface ($\approx 3.8 \text{ \AA}$), due mainly to thermally activated capillary-waves. We should point out, however, that this resolution is comparable to the diameter of one cesium ion (3.2 Å) or a single water molecule ($\sim 3 \text{ \AA}$), and therefore our experimental distributions constraint deviations from RPB theory to very short-range variations involving one, at most two, water molecules or cesium ions. If the actual ionic distribution is nonmonotonic, departures from RPB theory are even more constrained as it follows from the discussion in Figure 11.

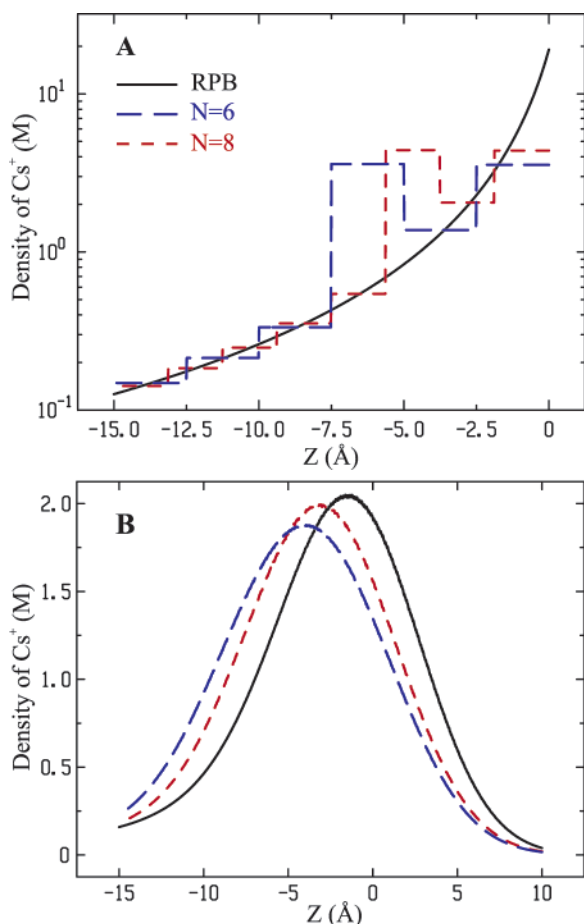


Figure 11. (A) Solid line corresponds to the RPB profile at bulk concentration 10^{-3} M. Steplike functions preserve the integral (up the first 15 Å) of the continuous RPB distribution. (B) Corresponding convolved distributions with a Gaussian of width $\Gamma = 3.8$ Å.

Our results show that theoretical effects that are usually suggested to modify PB theory, such as finite ion-size, in-plane modulations of surface charge density, hydration forces, short-range interactions, the roughness of the surface or image charges are not necessary to describe the experimental data. This is not to be understood as implying that such effects are not present, but rather that their significance is entirely limited to a

characteristic spatial distance of the order of ≈ 4 Å or less. As for claims based on the modification of PB by hydration forces (see for example, ref 12), our experimental results conclusively rule out the possibility of modifications of PB within the 10–20 Å range from the interface and confine such corrections, if present, to within the first 3–4 Å from the interface as discussed. Although the experimental counterion distributions are well described within the RPB theory, we point out that the reflectivity and GIXD hint at water restructuring at the interface. Future theoretical or numerical work may clarify this issue.

A recent report analyzing the accuracy of PB near charged liquid–liquid interfaces by the use of X-ray surface sensitive techniques shows that ion distributions are well described by PB at concentrations of 10 mM, but marked deviations are found at higher concentrations (of the order 100 mM), where ion–ion correlations have to be included in the theoretical analysis.⁵⁰ We did not perform anomalous reflectivity for concentrations above 10 mM, so we are not able to provide ionic distributions for these concentrations. We point out, however, the good agreement found for the integrated quantities at these concentrations (Figure 10B), which provides an example of integrated quantities possibly hiding deviations from actual distributions as pointed out in the Introduction.

The results presented in this study enhance our understanding of the electrostatics in aqueous media, and also show the strength of surface sensitive X-ray synchrotron techniques in obtaining high-resolution data.

Acknowledgment. We thank D. S. Robinson and D. Wermeille for technical support at the 6-ID beamline. The Midwest Universities Collaborative Access Team (MUCAT) sector at the APS is supported by the U.S. Department of Energy, Basic Energy Sciences through the Ames Laboratory under Contract No. W-7405-Eng-82. Use of the Advanced Photon Source is supported by the U.S. Department of Energy, Basic Energy Services, Office of Science, under Contract No. W-31-109-Eng-38. The work of A.T. is partially supported by NSF Grant DMR-0426597.

LA053400E

(49) Bowick, M. J.; Travestet, A. *Phys. Rep.* **2001**, *344*, 255.

(50) Luo, G. M.; Malkova, S.; Yoon, J.; Schultz, D. G.; Lin, B. H.; Meron, M.; Benjamin, I.; Vanysek, P.; Schlossman, M. L. *Science* **2006**, *311*, 216 (This Report became available to us after the submission of this manuscript).